International Journal of Heat and Mass Transfer 52 (2009) 971–985

Contents lists available at ScienceDirect

International Journal of Heat and Mass Transfer

journal homepage: www.elsevier.com/locate/ijhmt

Experimental study of multi-hole cooling for integrally-woven, ceramic matrix composite walls for gas turbine applications

Fengquan Zhong [a], Garry L. Brown [b,*]

[a] LHD, Institute of Mechanics, Chinese Academy of Sciences, Beijing 100190, PR China
[b] Department of Mechanical and Aerospace Engineering, Princeton University, Princeton, NJ 08544, USA

ARTICLE INFO

Article history:
Received 7 July 2007
Received in revised form 22 April 2008
Available online 14 October 2008

Keywords:
Integrally-woven ceramic matrix composite
Cooling effectiveness
Reynolds number
Blowing ratio
Temperature ratio

ABSTRACT

In this paper, multi-hole cooling is studied for an oxide/oxide ceramic specimen with normal injection holes and for a SiC/SiC ceramic specimen with oblique injection holes. A special purpose heat transfer tunnel was designed and built, which can provide a wide range of Reynolds numbers (10^5~10^7) and a large temperature ratio of the primary flow to the coolant (up to 2.5). Cooling effectiveness determined by the measured surface temperature for the two types of ceramic specimens is investigated. It is found that the multi-hole cooling system for both specimens has a high cooling efficiency and it is higher for the SiC/SiC specimen than for the oxide/oxide specimen. Effects on the cooling effectiveness of parameters including blowing ratio, Reynolds number and temperature ratio, are studied. In addition, profiles of the mean velocity and temperature above the cooling surface are measured to provide further understanding of the cooling process. Duplication of the key parameters for multi-hole cooling, for a representative combustor flow condition (without radiation effects), is achieved with parameter scaling and the results show the high efficiency of multi-hole cooling for the oblique hole, SiC/SiC specimen.

1. Introduction

New integrally-woven, ceramic matrix composites (CMC) formed by the 3-dimensional weaving of fibers, which can be multi-hole cooled, offer the prospect of substantial combustion system gain and they are being developed for gas turbine applications. The aim is to reduce the coolant gas requirement for combustor liner cooling, as well as to increase the combustor inlet temperature. Cox et al. [1] and Mehta et al. [2] discuss potential applications of integrally-woven CMC materials for gas turbine combustor liners. With the development of weaving and processing techniques, a relatively large number of small holes through the CMC material can be easily provided with minimal cost penalty and, at the same time, the mechanical and thermal strength can be maintained. As an example, Fig. 1 is a photograph of the multi-holed surface of an all-oxide ceramic specimen.

A multi-hole cooling system (also called "effusion cooling"), which has a relatively large number of injection holes of small size[1], introduces a secondary cold flow into the primary hot flow through these holes as shown schematically in Fig. 2. The coolant is then carried downstream by the primary flow. With an optimal design of the cooling configuration and at a specific operating condition (Reynolds number of the system, blowing ratio, temperature ratio), most of the coolant will flow near the target surface so that a stable cool film can be formed over the surface, which separates the surface from the high temperature and large heat flux in the primary flow. Compared to traditional 3D film cooling with a few relatively large holes, a multi-hole cooling system is expected to have a higher cooling efficiency[2] and be able to achieve a more uniform surface temperature distribution because of its relatively large percentage of hole area (>1%) produced by a large number of small holes. To the authors' knowledge, little is known about the fluid mechanics and heat transfer in the application of such multi-hole cooled CMC systems. Zhong & Brown [3] studied multi-hole cooling for an oxide/oxide specimen and provided some preliminary results for the cooling effectiveness. Subsequently, the experimental facility was fully insulated and modified to enable a temperature ratio between free stream and coolant of up to 2.5 to be obtained. The present results greatly extend and supersede this early work and also include results for the SiC/SiC material with a different hole geometry and thermal properties.

* Corresponding author. Tel.: +1 609 258 6083; fax: +1 609 258 2404.
E-mail address: glb@Princeton.edu (G.L. Brown).

[1] The typical hole size for a multi-hole cooling system, which would have acceptable clogging behavior in gas turbine applications, is in the range of 0.5~1 mm, while the hole size for a typical 3D film cooling application is generally larger. For cooling applications with boundary layer flows, a multi-hole cooling system may have a ratio of hole length/width to boundary layer thickness in the range of 0.1 or less, whereas, film cooling has a hole size comparable to the local boundary layer thickness or larger.

[2] Compared with conventional film cooling for typical applications, which has a blowing ratio of approximately $M \sim 1$ to 2 or higher, the multi-hole cooling systems in these experiments have a significantly lower blowing ratio ($M \sim 0.8$) for a comparable cooling effectiveness.

0017-9310/$ - see front matter © 2008 Elsevier Ltd. All rights reserved.
doi:10.1016/j.ijheatmasstransfer.2008.08.008

Nomenclature

A	area
d	wall thickness
L	streamwise distance from the entrance to the $4'' \times 4''$ square test section of the tunnel to the leading edge of the cooling specimen (approximately 0.34 m)
I	momentum ratio defined as $\frac{(\rho v^2)_c}{(\rho u^2)_\infty}$
k	thermal conductivity
M	blowing ratio defined as: $\frac{(\rho v)_c}{(\rho u)_\infty}$
N	total mass flow rate ratio
P	pressure
P_h	hole to hole spanwise distance
Re	Reynolds number defined by the streamwise distance L and free stream velocity
S_h	hole to hole streamwise distance
T	temperature
t	time
Tu	turbulence level
uvw	velocity components
xyz	streamwise, normal, spanwise direction

Greek symbols

θ	cooling effectiveness defined as $\theta = \frac{T_{w_{no\text{-}cooling}} - T_{w_{with\text{-}cooling}}}{T_{w_{no\text{-}cooling}} - T_c}$
α	hole angle
ρ	density
δ	boundary layer thickness
η	non-dimensional temperature
β	percentage of the hole area
κ	temperature ratio defined as $\frac{T_\infty}{T_c}$
μ	dynamic viscosity
v	coolant mean injection velocity

Subscripts & superscripts

c	coolant
h	hole
w	wall
∞	free stream

Importantly, a multi-hole cooling system can provide a substantial backside cooling effect due to the heat convection to the backside coolant flow and the heat conduction through the wall. Thin wall, integrally-woven, CMC materials are, in fact, relatively conducting. (Compared with super-alloy walls with a thermal conductivity of approximately 100 W/m/K, CMC materials have a smaller thermal conductivity of 4∼15 W/m/K, but this value is still relatively large compared with many ceramics $k < 1$ W/m/K.) In their recent detailed numerical study, Zhong and Brown [4] addressed the importance of the backside cooling effect for a multi-hole oxide/oxide specimen and proposed a 3D coupled heat transfer model, which includes all heat transfer processes (except radiative heat transfer) in a multi-hole cooling system. Their DNS solutions show the significant effect of the backside cooling and their predictions of the cooling effectiveness agree well with the experimental results at the same Reynolds numbers and cooling conditions.

In this paper, multi-hole cooling is studied experimentally with a special purpose heat transfer tunnel. Two types of woven CMC materials have been investigated and the effects of blowing ratio, temperature ratio, Reynolds number, hole geometry and the thermal properties of the wall material are explored. Another objective of this study was to duplicate the cooling process for representative combustor flow conditions (in the absence of radiation effects) through parameter scaling but using the same material and geometry. For example, if we assume a maximum combustor mainstream temperature of approximately $T_\infty \sim 2400$ K[3], $T_c \sim 1000$ K for the coolant temperature, $U_\infty \sim 60$ m/s for the main-stream velocity and $P_\infty \sim 60$ atm for the static pressure, the heat transfer tunnel can be operated at values of temperature and pressure that are 1/6 of these values, i.e. at a tunnel temperature of 400 K, a coolant temperature of 167 K and a tunnel pressure of 10 atm. This scaling enables the density[4] and density ratio (ratio of coolant to main-stream) to be the same as for an actual combustor flow. By using the same CMC material and geometry as in the actual combustor liner, the same Reynolds number (based on the characteristic dimension for the geometry of the liner material) can be obtained by adjusting the free stream velocity as follows.

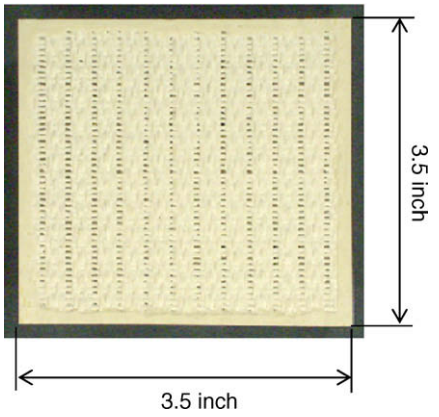

Fig. 1. Multi-holed surface of the oxide/oxide specimen.

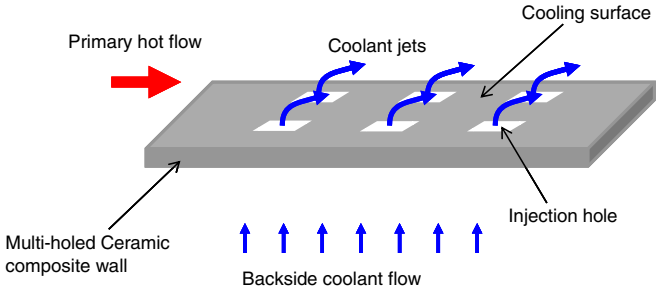

Fig. 2. Schematic diagram of a multi-hole cooling system.

With $\rho_{real} = \rho_{test}$, $d_{real} = d_{test}$ and assuming that $\frac{\mu_{test}}{\mu_{real}} \sim (\frac{T_{test}}{T_{real}})^{0.667}$, the same Reynolds number requires:

$$\frac{U_{test}}{U_{real}} = \left(\frac{T_{test}}{T_{real}}\right)^{0.667} \quad (1)$$

In this example, we have $U_{test} = 60(\frac{1}{6})^{0.667} = 18$m/s.

Thus for the same density ratio, and hole velocity to freestream velocity ratio, and the same Reynolds number based on hole size (same liner geometry) we would also require the same d/L or d/δ. Of course L or δwill vary with the application but the present scaling ensures a matching of the principal parameters, velocity ratio,

[3] The flow conditions used here are obtained with reference to proposed working conditions for a future turbine engine combustor, for example, a 2-D Trapped Vortex Combustor.

[4] The same density is based on the assumption of a perfect gas.

density ratio and Reynolds number and is based on a representative d/δ.

It is worth noting that the effect of radiation is not included in this duplication. It can be very important for a real combustor flow condition at high temperature and with significant concentrations of CO_2 or H_2O. It is well understood however, and the focus in the present work is on convective heat transfer.

This paper is organized as follows. The special purpose heat transfer tunnel is described in Section 2. In Section 3, we discuss the measurements and in Section 4 we present the results obtained for the oxide/oxide specimen with normal injection holes (Section 4.1) and the results for the SiC/SiC specimen with oblique holes (Section 4.2). The particular effects of blowing ratio, temperature ratio and Reynolds number are discussed in these sections. Finally, in Section 5, we summarize the conclusions that can be drawn from the experimental results.

2. The experimental facility

A special purpose heat transfer tunnel was designed to meet two principal requirements: (1) the duplication of Reynolds number, coolant and free stream density ratio and velocity ratio applicable for ceramic matrix composite (CMC) specimens proposed for a multi-hole cooling system for gas turbine applications; (2) a wide range of Reynolds number to provide both an overlap with DNS calculations at low Reynolds number [4] and also the highest Reynolds number of the applications.

Fig. 3. Photograph of the heat transfer tunnel with insulation.

The heat transfer tunnel consists of a closed-circuit tunnel system insulated with mineral wool pipe/elbow insulation and a secondary flow (coolant flow) injection system. Fig. 3 is a photograph of the tunnel with insulation and Fig. 4 is a schematic diagram showing the key elements of the tunnel. With air used as the working fluid, the tunnel can be operated at a pressure of sub-atmospheric to 20 atm, at a temperature of 300–400 K and a velocity of 10–30 m/s. The secondary flow can be cooled through a heat exchanger filled with dry-ice or liquid nitrogen and a maximum temperature ratio of the primary flow to the coolant of approximately 2.5 can be obtained.

The pipe section of the tunnel is made of 35.6 cm (14″) O.D. stainless steel pipe and connected with raised-face, weld-neck flanges. A pressure relief system consisting of a pressure relief valve and two back pressure regulators is installed to avoid overpressure conditions and to adjust the tunnel pressure and keep it close to constant when coolant gas is injected into the tunnel.

The contraction has an area ratio of 8.6:1 and a stainless steel, round to square transition liner was built and welded inside the contraction. It makes a smooth contour transition from a circular to square test section. The diffuser has the same area ratio and a similar transition from a square to circular cross-section. Honeycombs and screens are mounted in the settling chamber to achieve adequate flow quality. Measurements obtained by hotwire anemometer showed an approximately 2% free stream turbulence level for Reynolds number of 200,000∼2,000,000. (A reduction in free stream turbulence level will be achieved with the installation of turning vanes which have yet to be installed.)

Particular attention was paid to the design of the test section to accommodate the CMC specimen and secondary cooling flow. The test section has a 10.2 × 10.2 cm (4″ × 4″) square cross-section and Fig. 5 is a photograph showing the inside structure of the test section with a side wall and end flange removed. The test section has a double floor structure. The top and bottom outer walls (the "pressure" walls) were made of 2.54 cm (1″) thick, 304 stainless steel plates. The two inner walls form the 4″ × 4″ square section and the lower wall is also used for the mounting of different cooling specimens. Surfaces of the inner walls were mill finished to a roughness of approximately 1 micron. A backside cavity (20.3 cm × 10.2 cm × 5.1 cm) is formed by the two lower walls,

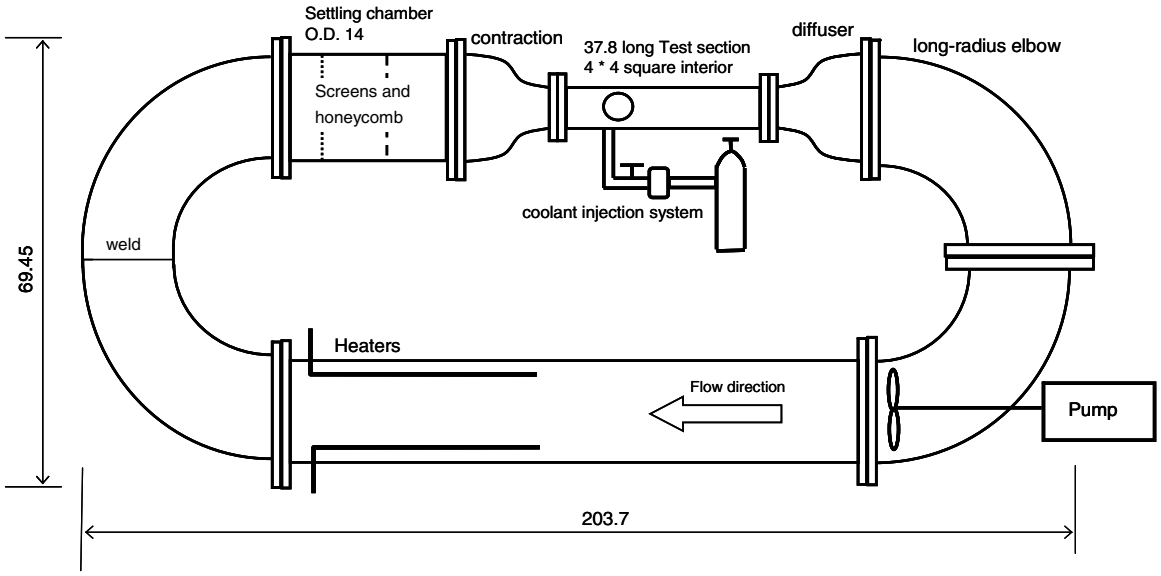

Fig. 4. Schematic diagram of the heat transfer tunnel (unit: inches).

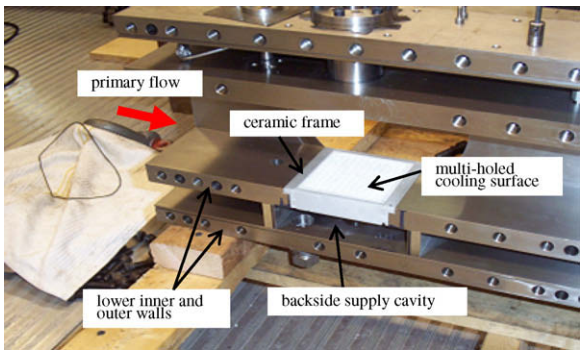

Fig. 5. Test section with a side wall and end flange removed.

the two side walls and two additional pieces, as shown in Fig. 5. Additional insulation is applied on the cavity wall to reduce the heat loss through the walls.

The tunnel is driven by a variable speed 20 hp pump, which was fabricated into an elbow section. To obtain a free stream temperature of 400 K, a heating system is required. It consists of six round, tubular, heater rods arranged as three sets of two in series and connected to each phase of a 480-volt, three-phase supply. The heating is controlled by a microprocessor-based temperature controller with pre-set temperature values. With tunnel insulation, the heating system is very efficient; only 3∼4 h are required for the tunnel (including the steel walls) to be heated to 360∼390 K.

The secondary flow injection is accomplished using a separate high pressure air supply. Fig. 6 shows the secondary flow injection system. It consists of a gas cylinder supply, a flow regulator, an on/off ball valve, a metering valve and a heat exchanger. The output pressure of the flow regulator is typically 689 KPa (100 psi) higher than the tunnel pressure and a metering valve is used to control the coolant flow rate. A maximum volume flow rate for the present system is approximately 0.008 m^3/s (17CFM) and a range of values of the blowing ratio M from 0.1 to 2.0 can be obtained.

To obtain coolant flow at low temperature (less than the gas cylinder temperature), the coolant gas is cooled in a heat exchanger. The heat exchanger consists of 1.27 cm diameter copper coils submerged in dry-ice (1.3 cm diameter granules) or in liquid nitrogen. The container for the dry-ice or liquid nitrogen was a heavy-duty cooler wrapped with fiber-glass insulation. This simple cooling configuration was found to be very effective and with dry-ice, a decrease of 60∼80 K in coolant temperature was obtained and with liquid nitrogen, a coolant temperature of 160 K was readily obtained.

3. Flow/thermal measurements

Fig. 7 shows the locations of the pressure and temperature measurements. The differential pressure between the static pressure in the settling chamber P_0 and in the test section P_1 is used to determine the free stream velocity. A type-K thermocouple probe was mounted in the settling chamber for the measurement of free stream static temperature. Fig. 8 (a) and (b) shows the measured free stream turbulence level at different Reynolds numbers and on different days and a level of approximately 2% was found for all flow conditions.

Type-K thermocouples with a wire diameter of 0.127 mm were mounted on the cooling surface of the specimens at different streamwise locations for the surface temperature measurements. (Their locations for each specimen are described in later sections.) A Pitot probe was traversed across the boundary layer above the cooling surface to obtain the mean velocity profile $u(y)$ where the mean density was obtained from the local temperature measured at the same location. The tip of the probe was made of stainless steel tubing and flattened to a height of approximately 0.66 mm. A temperature probe traversed with the Pitot probe was used to measure the mean temperature profile $T(y)$.

Thermocouple probes were mounted in the backside supply cavity for the measurement of the backside coolant temperature T_c and a pressure tube was used for the measurement of the backside cavity pressure P_c. The uniformity of the temperature field in the backside cavity at different cooling conditions was checked by comparing measured temperatures at different locations in the backside cavity and a mean value of these measured temperatures was used as the backside cavity temperature T_c. The differen-

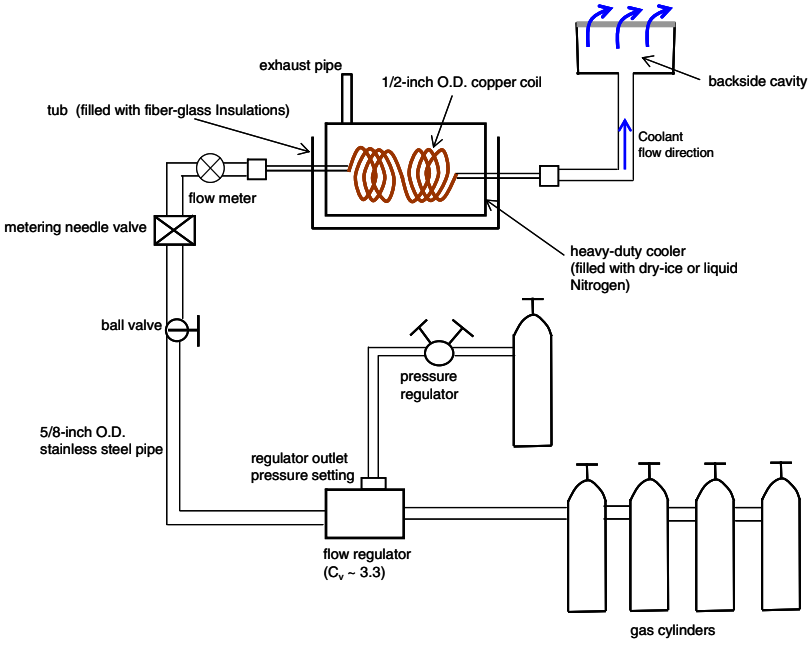

Fig. 6. The coolant injection system.

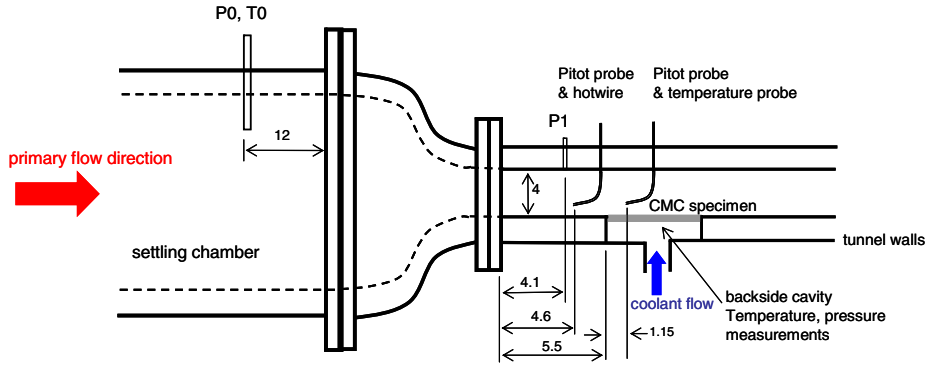

Fig. 7. Locations of the pressure, temperature and velocity measurements (unit: inches).

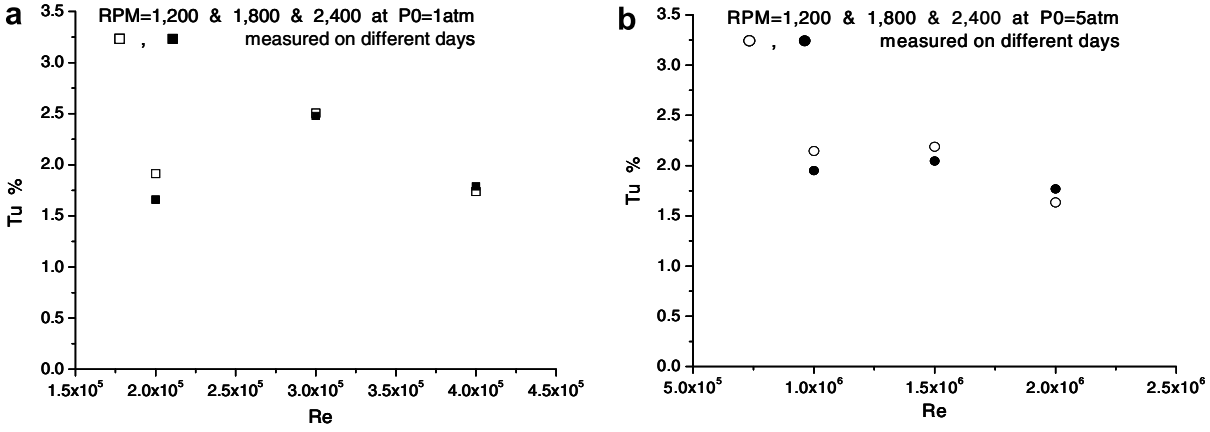

Fig. 8. Turbulence level in the free stream at different Reynolds numbers (a) *Re*: $2 \times 10^5 \sim 4 \times 10^5$; (b) $1 \times 10^6 \sim 2 \times 10^6$.

tial pressure between the backside cavity pressure P_c and the static pressure of the primary flow P_1 was measured with a Baratron pressure transducer with an accuracy of approximately 1.3 Pa and used to determine a mean injection velocity through the holes. Assuming uniform flow in the injection holes, no loss in the total pressure and constant density, this differential pressure can be used to obtain an injection velocity through the holes.

$$v_c = \sqrt{2RT_c \frac{P_c - P_1}{P_c}} \tag{2}$$

With v_c and T_c known, the value of blowing ratio M and momentum ratio I can be determined from their definitions.

A high-pressure gas flow meter with a range of 0.0094 m^3/s (20CFM) was installed in the supply line for the measurement of the total volume flow rate $\dot{Q}_c$. Knowing the total hole area of the specimen, the mean injection velocity v_c can also be determined from the measured volume flow rate. The mean injection velocities obtained from Eq. (2) and from the measured volume flow rate were compared and the difference found to be less than 5% when the volume flow rate was less than 0.004 m^3/s, corresponding to a blowing ratio of approximately 1.0.

The cooling effectiveness is defined as a ratio of measured temperature differences: $\theta = \frac{T_{w_{no\text{-}cooling}} - T_{w_{with\text{-}cooling}}}{T_{w_{no\text{-}cooling}} - T_c}$, which has a range of 0–1 with 1 representing the maximum cooling effect and 0 representing no-cooling effect.

The uncertainty in the data was determined by the accuracy of the instruments and the variations in the data obtained on different days. The uncertainty was found to be approximately $\leqslant \pm 0.04$ for the cooling effectiveness θ and $\leqslant \pm 0.05$ for the blowing ratio M. Fig. 9 shows the cooling effectiveness θ as a function of the blowing ratio

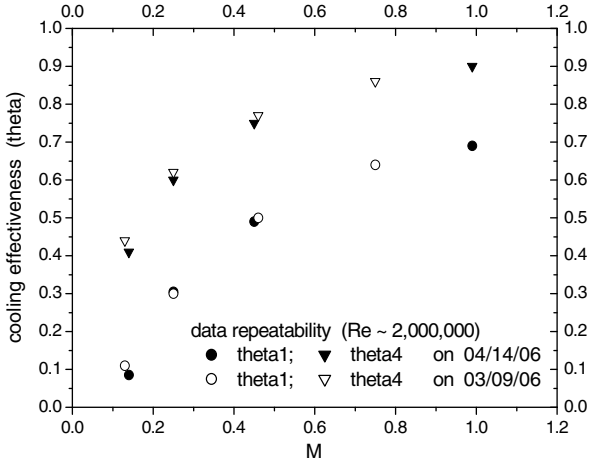

Fig. 9. Cooling effectiveness θ vs. blowing ratio M (measured on different days).

M at two streamwise locations for the SiC/SiC specimen obtained on different days; a satisfactory repeatability in θ is found.

4. Experimental results

4.1. Cooling effectiveness for a multi-hole oxide/oxide ceramic specimen

4.1.1. Thermal and geometrical properties of the oxide/oxide specimen

Fig. 1 is a photograph of the oxide/oxide specimen, which is comprised of a matrix made of half Alumina (AL_2O_3) and half

Table 1
Geometrical and thermal properties of the oxide/oxide specimen

Wall material	Thermal conductivity (W/m/K)	~4.5	Density (kg/m^3)	4000	Specific heat (J/kg/K)	700
Hole geometry & arrangement	Typical hole size (mm) (length, width)	1.4, 0.9	S_h, P_h (mm)	6.3, 2.8	Hole angle	90°
	Percentage of hole area	~7%	Wall thickness d (mm)	1.5	Surface roughness r (mm)	~0.55

Monazite ($LaPO_4$) and Alumina fibers. It was designed and manufactured by the Boeing Rockwell Science Center (RSC). The AL_2O_3/$LaPO_4$ composite has been tested for extended operation at temperatures exceeding 1700 K. Potential gas turbine applications of the oxide/oxide specimen and its thermal properties are discussed in detail by Cox et. al. [1]. Table 1 gives geometrical details (based on average measurements) and the thermal properties of the specimen. It can be seen from Fig. 1 that the surface has relatively poor hole uniformity. Hence, the cooling effectiveness was measured downstream of both typical holes and of a small hole and the results at these locations are compared. A significant roughness of the multi-hole surface due to the weave of the fibers and the manufacturing process is also evident from Fig. 1. The average roughness height was measured and was approximately $r = 0.55$ mm.

4.1.2. Experimental aspects for the measurements with multi-hole cooling

The insulated tunnel was first heated to the required temperature for 3 ~ 4 hours before any cooling experiments. The temperature difference measured in the free stream and on the ceramic surface was used to determine when thermal equilibrium was reached. The tunnel pressure would increase when coolant gas is injected into the tunnel during the cooling process unless the tunnel pressure is controlled. With two back pressure regulators (one for coarse adjustment, the other for fine adjustment), the tunnel pressure was kept practically constant during the injection. The coolant injection is supplied for a few minutes at each blowing ratio and during the first minute or so the system reaches a new equilibrium (as shown in Fig. 10 (e)). Typically, the heater is turned off during a cooling experiment to provide reliable measurements of the free stream temperature.

Fig. 11 is a sketch showing the locations of surface temperature measurements and the locations for the measurements of the temperature and velocity profiles across the boundary layer (Table 1 provides geometrical dimensions). Thermocouples 1, 2, 3 and 4 are located on the centerline of the specimen and at different streamwise locations. Thermocouple 5, located downstream of a typical small hole and at the same streamwise location as thermocouple 2, is used to indicate the effect of different hole sizes on cooling performance.

Fig. 10(a) shows the measured surface temperatures (at location 1 and 2) and Fig. 10(b) the differential pressure $P_c - P_1$ for a typical cooling experiment ($Re \sim 4{,}000{,}000$[5] and temperature ratio of 1.2). Fig. 10(c) and (d) presents the tunnel pressure and calculated blowing ratio, M. From Fig. 10(a), the initial temperature difference (before the injection of the coolant, time < 12 s), between the free stream temperature and the ceramic surface temperature is less than 5 K, which indicates that the tunnel system had reached thermal equilibrium with a small heat loss through the tunnel wall. The injection begins at $t = 12$ s, and ends at approximately $t = 250$ s. The injection for approximately 4 min was found to be more than long enough for the surface to reach a new thermal equilibrium with the cooling flow. Actually, the new thermal equilibrium is developed at approximately $t = 100$ s, since the cooling effectiveness curve given in Fig. 10(e) becomes almost flat after $t = 100$ s. Fig. 10(b) shows the average pressure drop through the injection hole, which is approximately $\Delta P \sim 1.1$ kPa (8.2 torr); the range of the pressure ratio $\frac{\Delta P}{P_t}$ (where, P_t is the static pressure of the test section) for both the oxide/oxide specimen and SiC/SiC specimen varies from approximately 10^{-4} at low Reynolds numbers ($\leqslant$200,000) and small blowing ratios ($M \leqslant 0.2$) to approximately 10^{-2} at high Reynolds numbers ($\geqslant$4000,000) and large blowing ratios ($M \geqslant 1$). The blowing ratio curve in Fig. 10(d) and the tunnel pressure curve in Fig. 10(c) show that the two back pressure regulators provide good control of the static pressure in the tunnel during injection after a settling time of approximately 100 s. The data obtained between $t = 125$ s and $t = 250$ s are used to determine the mean value of the cooling effectiveness θ and blowing ratio M.

4.1.3. Results and discussion

The cooling effectiveness θ and its spatial variation on the upper surface are of primary interest. Fig. 12 gives the measured cooling effectiveness at thermocouple locations 1–5, as indicated in Fig. 10, for $Re \sim 4{,}000{,}000$ and a temperature ratio of 1.2. Three conclusions can be drawn from these results: (1) the overall cooling efficiency of this oxide/oxide specimen is relatively high since, at $M \sim 0.5$, the cooling effectiveness at all locations was larger than 0.6; (2) the measurements of cooling effectiveness at locations 2, 3 and 4 are close to each other (the difference is less than 0.1), which indicates a close-to-uniform temperature distribution downstream of the 5th row of holes; (3) the difference between θ_2 and θ_5 (i.e. due to the significant difference in hole size) decreases as blowing ratio increases and the maximum difference between them is less than 0.2. This shows that the variation in the size of the holes is not a critically important factor for the cooling performance of the present oxide/oxide specimen.

Fig. 13 (a)–(d) shows the results for the cooling effectiveness as a function of blowing ratio at locations 1, 2, 3 and 4 at different Reynolds numbers (obtained with different tunnel pressures) and at a temperature ratio of approximately 1.2. They show the initial increase in the cooling effectiveness with blowing ratio and also show that, for $M > 0.6$, the cooling effectiveness does not increase very much with further increase in M. This could indicate that a local film of coolant has been established above the surface at large blowing ratios and the measured temperature profiles above the cooling surface shown in Figs. 14 and 15 support this explanation. Fig. 13 (a)–(d) also shows the weak dependence on Reynolds number (a small reduction in effectiveness with increasing Reynolds number) and that the Reynolds number effect is more significant at small blowing ratios and diminishes at large blowing ratios. This can be explained by the combined effect of the backside cooling and heat conduction in the wall. When the backside cooling effect is significant (especially for small blowing ratios), the increase in the system Reynolds number, due to the increase in pressure and density in both the primary flow and the backside flow, increases the heat flux through the wall and causes the temperature drop across the wall to become relatively larger, which raises the upper surface temperature and reduces cooling effectiveness. The numerical solution obtained by the 3D heat transfer model discussed in Zhong & Brown [4] also shows the decrease in cooling effectiveness with Reynolds number at two blowing ratios ($M = 0.24$ and $M = 0.43$). In their paper, they discussed the Reynolds number

[5] This flow condition is obtained at a tunnel pressure of 10 atm, a temperature of ~360 K and a tunnel speed of 20 m/s.

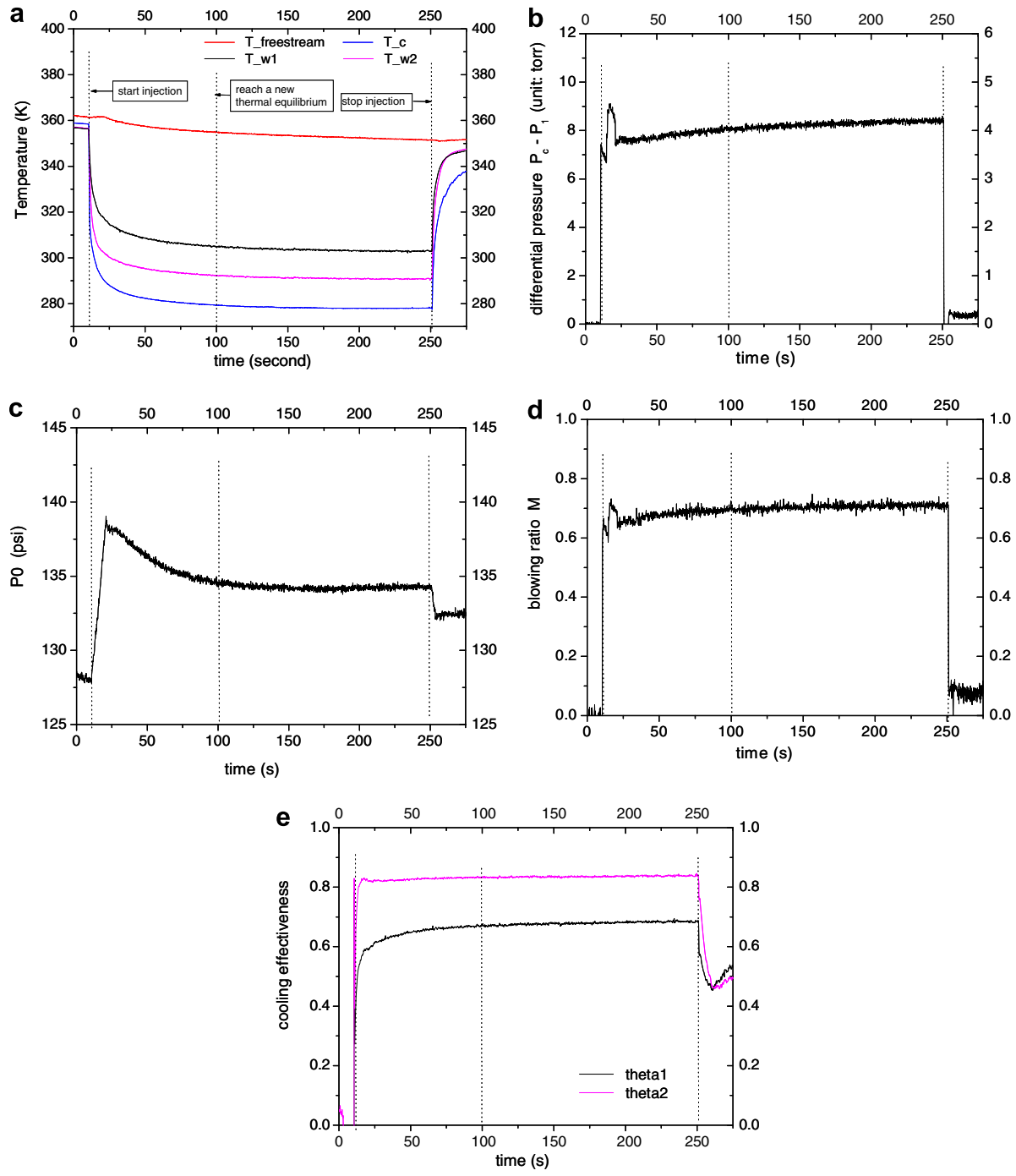

Fig. 10. Change of pressure, temperature etc. with time for $Re \sim 4{,}000{,}000$ and $M \sim 0.7$ (a) temperature; (b) differential pressure $P_c - P_1$; (c) tunnel pressure; (d) blowing ratio M; (e) cooling effectiveness.

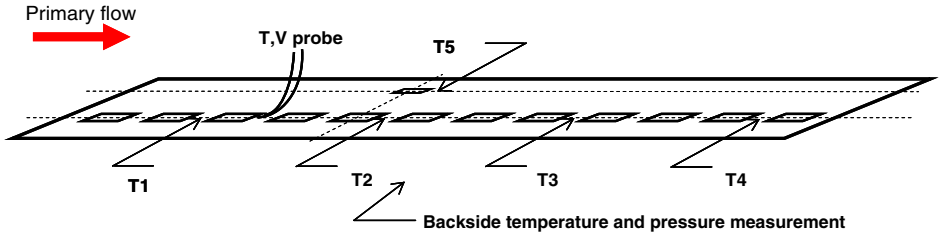

Fig. 11. Schematic diagram showing locations of the surface temperature and velocity/temperature profile measurements.

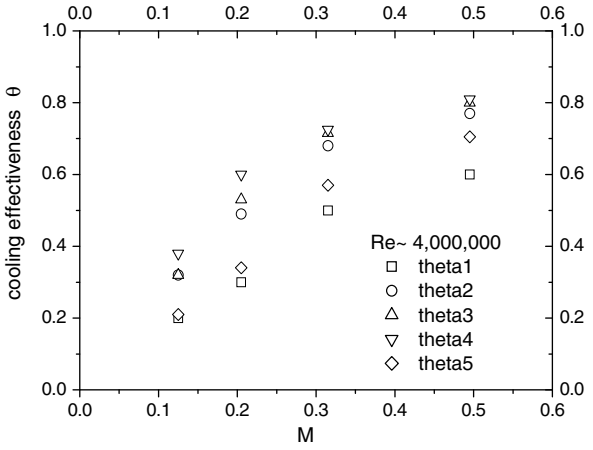

Fig. 12. Cooling effectiveness vs. blowing ratio at different locations.

effects in terms of a Biot number $\frac{hd}{k}$ and indicated that the cooling effectiveness decreases as the Biot number increases.

Fig. 14 shows the measured temperature profiles obtained from the traverse of the temperature probe across the boundary layer with and without cooling for $Re \sim 2{,}000{,}000$. With the insulation on the test section and on the backside cavity wall, the difference between the free stream temperature T_0 and the surface temperature T_w is only 6 K when there is no cooling, indicating a relatively small heat loss through the walls. To eliminate the remaining effect (i.e. the initial heat flux through the tunnel wall), the temperature profile without cooling is used as a reference profile and a non-dimensional temperature η, as in Eq. (3), is used to define the temperature profile with multi-hole cooling.

$$\eta(y) = \frac{T(y)_{\text{with-cooling}} - T(y)_{\text{no-cooling}}}{T(y \sim 0)_{\text{with-cooling}} - T(y \sim 0)_{\text{no-cooling}}} \tag{3}$$

Based on Eq. (3), Fig. 15 (a) and (b) shows the non-dimensional temperature profiles $\eta(y)$ at two Reynolds numbers $Re \sim 400{,}000$ and $Re \sim 2{,}000{,}000$. It can be seen that the corresponding temperature boundary layer thickness increases as the blowing ratio increases, and at lower blowing ratios, there exists a significant temperature gradient (heat flux) at the surface, whereas, the measured temperature profiles show a local approach towards zero temperature gradient at the wall for large blowing ratios ($M > 0.7$). This small temperature gradient could be expected to imply the formation of a local film of coolant as discussed above in the context of Fig. 13. The formation of such a local film is the objective for an efficient multi-hole cooling system. Fig. 16 (a) and (b) shows the normalized velocity profiles for the two Reynolds numbers. The mean velocity near the wall decreases with increasing blowing ratio due to the effect of the coolant jets. We note in passing that the effect of the coolant jet may also be seen from the profiles of velocity gradient $(\frac{\partial u^*}{\partial y}, u^* = \frac{u}{U_\infty})$ at different blowing ratios as shown in Fig. 17 (a) and (b) for the two Reynolds numbers. In both figures, profiles with cooling show an evident peak away from the wall and the location of the peak moves further away from the wall as blowing ratio M increases. This peak region in the profiles indicates a shear layer that is caused by the interaction between the coolant jet and the primary flow as the jets penetrate further into the boundary layer with increasing blowing ratio.

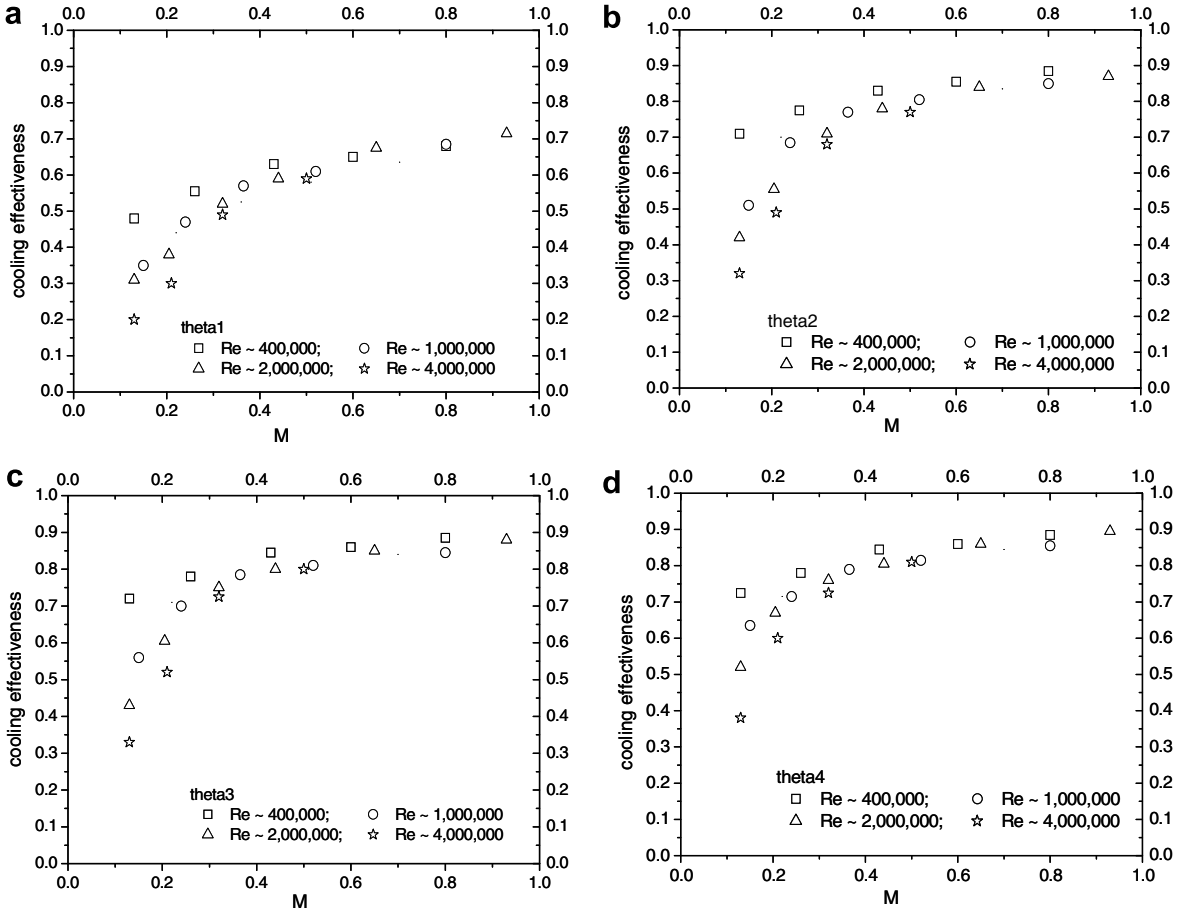

Fig. 13. Cooling effectiveness vs. blowing ratio at different Reynolds numbers (a) location 1; (b) location 2; (c) location 3; (d) location 4.

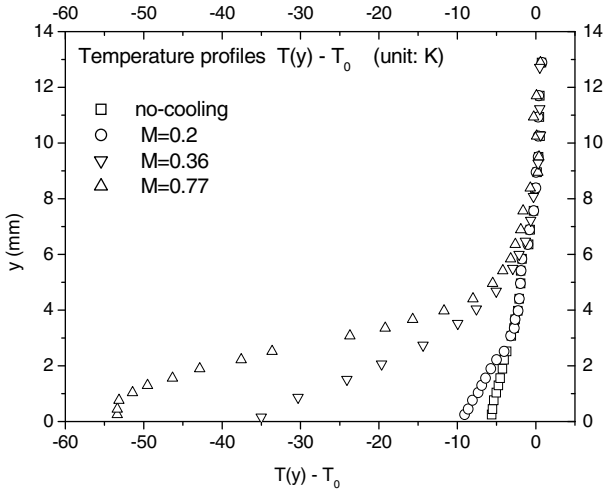

Fig. 14. Temperature profiles with/without cooling for *Re* ~ 2,000,000.

4.2. Cooling effect for a multi-hole SiC/SiC ceramic specimen

4.2.1. The thermal and geometrical properties of the SiC/SiC specimen and measurement aspects

The second CMC specimen is a SiC-based ceramic composite. The SiC ceramics are light weight (the density is only one third of the density of a typical Ni-based super alloy) and the specimen formed with a 3D woven integral-structure can achieve a high matrix density, which implies a larger thermal conductivity than the oxide/oxide CMC and superior mechanical and thermal strength. The multi-hole SiC/SiC specimen was also designed and manufactured by the Boeing Rockwell Science Center (RSC). Mehta et. al. [5] described the mechanical and thermal properties of the SiC/SiC composite in detail. Fig. 18 is a photograph showing portion of the woven SiC material with red/green boxes indicating hole locations and Fig. 19 shows the geometry of the oblique holes and their staggered arrangement. The pair of opposing oblique holes is formed by inserts into the weave prior to infusion by the matrix material. This oblique hole configuration is designed to substantially increase the contact surface between the wall and the coolant and is expected to give a higher cooling effectiveness and a more uniform surface temperature distribution. Table 2 gives geometrical details and thermal properties of the multi-hole specimen. Compared with the oxide/oxide specimen, which had poor hole uniformity, the holes in the SiC/SiC specimen were much more uniform in size and spacing. The surface roughness was also much smaller than that for the oxide/oxide specimen and an average roughness height of approximately 0.15 mm was found.

The operation/measurement procedure was similar to that for the oxide/oxide specimen. Thermocouples were mounted on the surface for surface temperature measurements and a temperature probe and Pitot probe were traversed across the boundary

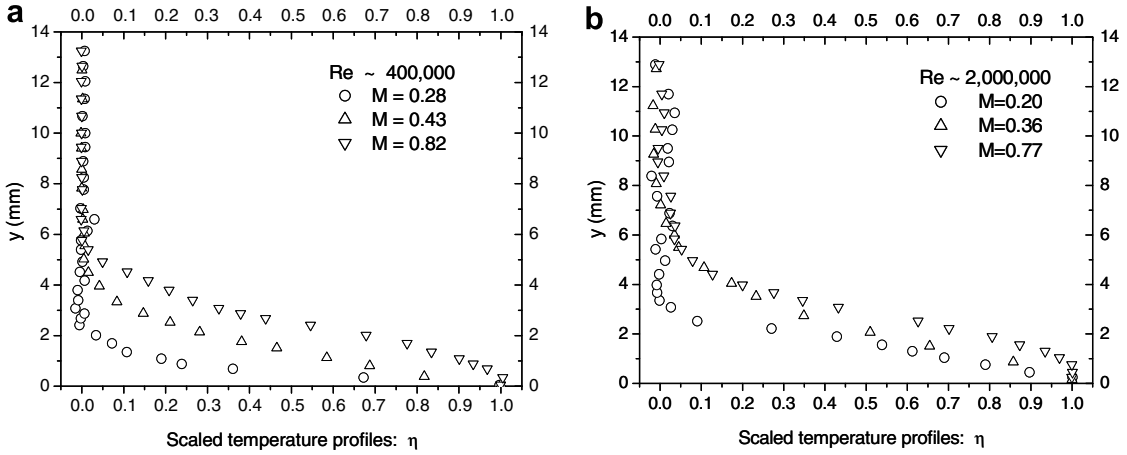

Fig. 15. Normalized temperature profiles at different blowing ratios (a) Re ~ 400,000; (b) Re ~ 2,000,000.

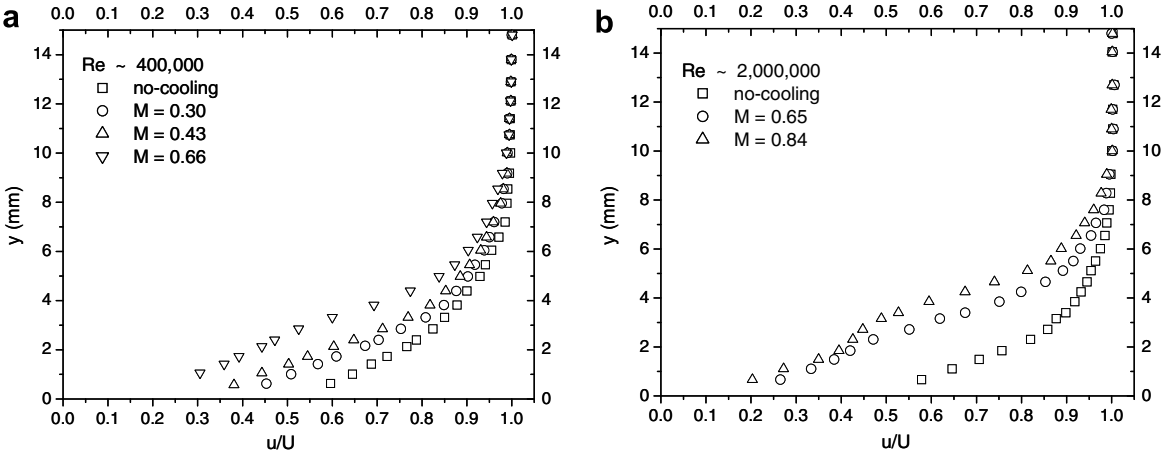

Fig. 16. Normalized velocity profiles at different blowing ratios (a) *Re* ~ 400,000; (b) *Re* ~ 2,000,000.

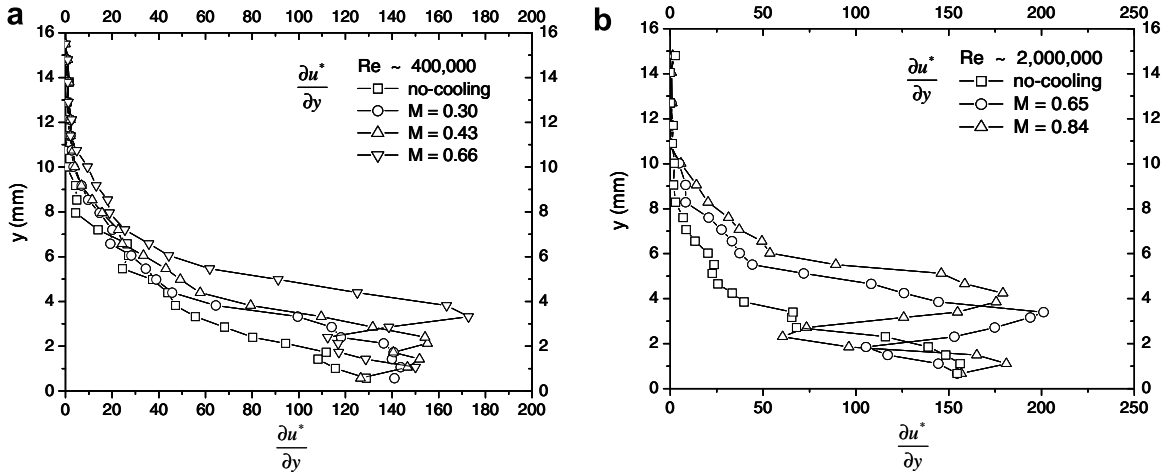

Fig. 17. Velocity gradients at different blowing ratios (a) $Re \sim 400{,}000$; (b) $Re \sim 2{,}000{,}000$.

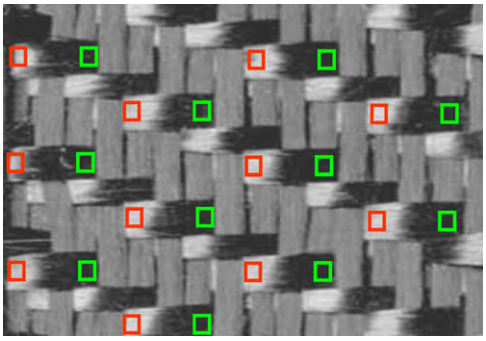

Fig. 18. Multi-holed SiC/SiC surface (red and green boxes indicate the location of the pair of oblique holes). (For interpretation of the references to color in this figure legend, the reader is referred to the web version of this paper.)

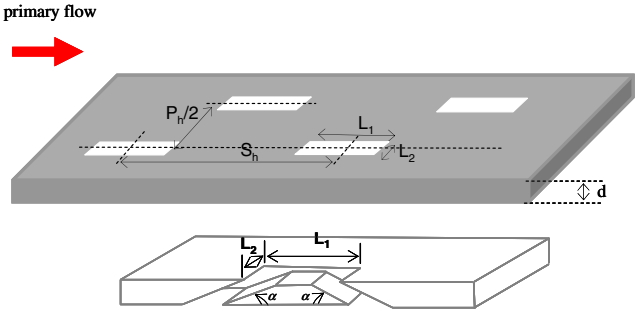

Fig. 19. Sketch of the multi-holed surface with dimensions of the holes dimension.

layer for temperature and velocity profile measurements. Fig. 20 shows the location of the measurements for surface temperatures and for the mean temperature and velocity profiles. The backside cavity temperature and pressure were also measured to determine the mean injection velocity and the temperature of the coolant.

4.2.2. Results at small temperature ratios ($\kappa = 1.1 \sim 1.2$)

The results for the cooling effectiveness θ at four streamwise locations (as shown in Fig. 20, *T*1–*T*4) for $Re \sim 4{,}000{,}000$ are given in Fig. 21. From the figure, it is evident that the cooling system for the SiC/SiC specimen has a high overall cooling efficiency. Similar to the oxide/oxide multi-holed surface, the cooling effectiveness does not show significant improvement (less than 0.15) from location 2 to location 4 at $M > 0.2$, which indicates an approach to a uniform distribution of surface temperature downstream of the 5th row of staggered holes. It is interesting that cooling effectiveness at location 3 and location 4 (θ_3 and θ_4) exceeds 0.7 for $M \geqslant 0.45$ and reaches a value as high as 0.9 at $M \sim 1.0$.

The cooling effectiveness at location 1 and location 3 at different Reynolds numbers is shown in Fig. 22 (a) and (b). From the figure, no significant Reynolds number dependency is found (within measurement errors), even at small blowing ratios. This indicates some difference in the heat transfer process between the SiC/SiC specimen and the oxide/oxide specimen. With a larger thermal conductivity (at least three times larger than that of the oxide/oxide specimen) and a thinner wall, the SiC/SiC specimen is a relatively conducting wall, which results in less temperature drop across the wall than for the oxide/oxide case. Hence, when heat convection in the flow regions is increased due to increased tunnel pressure, the temperature drop across the wall and the corresponding increase in the upper surface temperature is much smaller than that for the oxide/oxide specimen, which leads to a substantially weaker *Re* dependence. This corresponds with a lower Biot number. From the figures, it is also found that there is only a small increase in cooling effectiveness at blowing ratios of $M > 0.8$. This indicates that a local coolant film is being established over the surface at the higher blowing ratios and this is confirmed by the measured temperature profiles shown in Fig. 24.

It is of interest to compare the cooling effectiveness of the two specimens (oxide/oxide and SiC/SiC) at the same streamwise locations and at the same cooling conditions. Due to different percentages of hole area for the two specimens, however, the blowing ratio *M* is not a good parameter to be used in the comparison. Rather, we

Table 2
Geometrical and thermal properties of the SiC/SiC specimen

Wall material	Thermal conductivity (W/m/K)	~15	Density (kg/m^3)	3000	Specific heat (J/kg/K)	750
Hole geometry & arrangement	Hole size (mm) (length, width)	0.5, 1.0	S_h, P_h (mm)	9, 5	Hole angle	13°
	Percentage of hole area	~4.5%	Wall thickness *d* (mm)	1.0	Surface roughness *r* (mm)	~0.15

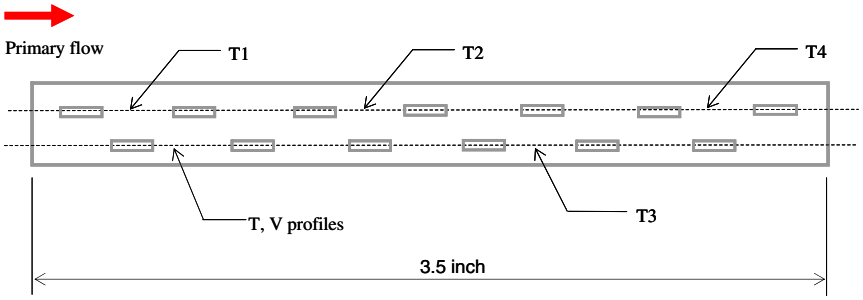

Fig. 20. Temperature and velocity measurement locations.

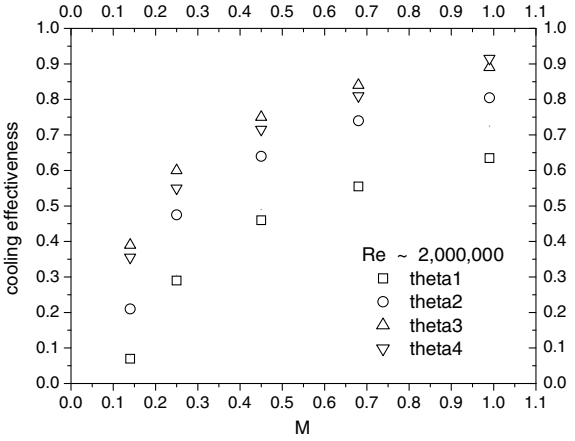

Fig. 21. Cooling effectiveness vs. blowing ratio at different locations ($Re \sim 4{,}000{,}000$).

choose the total mass flow rate ratio N, which is defined as: $\frac{(\rho v)_{\text{coolant}} A_h}{(\rho u)_\infty A_w}$, as the key parameter, where, A_h represents the total area of the holes and A_w is the surface area of the specimen, i.e. $N = \frac{(\rho v)_{\text{coolant}}}{(\rho u)_\infty}\beta$, where β is the percentage of hole area on the surface. Fig. 23 (a) and (b) gives the cooling effectiveness θ vs. N at an upstream location and a downstream location at $Re \sim 2{,}000{,}000$. For both locations, the SiC/SiC specimen shows a higher cooling efficiency than the oxide/oxide specimen. This can be understood by considering the difference in thermal properties and hole geometries for the two specimens. The SiC/SiC specimen has a larger thermal conductivity, which makes the material more conducting and makes the cooling effect, especially the backside cooling, more efficient. The SiC/SiC specimen also has an oblique twin-hole geometry. The oblique hole, which has a longer passage through the wall, increases the contact surface between coolant and the wall and makes the heat exchange inside the hole more effective. (This explanation is supported by numerical studies in Zhong [6].) In this experimental work, it was not possible to keep the geometry fixed and change the material or vice versa.

Fig. 24 (a) and (b) shows the temperature and velocity profiles across the boundary layer at the location indicated in Fig. 20. A local approach towards a very small temperature gradient near the wall can be seen in the temperature profile at large blowing ratio ($M \sim 0.72$), which supports the view expressed above that a local film of coolant is being established above the surface at the higher blowing ratios. The velocity profiles show the deficit near the wall caused by the coolant jet. Fig. 24 (c) shows profiles of velocity gradient $\frac{\partial u^*}{\partial y}$ across the boundary layer with cooling and the peak in the velocity gradient away from the wall is also observed at a blowing ratio of $M \sim 0.72$.

4.2.3. Results at large temperature ratios (κ = 1.5~1.7 & 2.1~2.4)

With dry-ice or liquid nitrogen in the heat exchanger used to cool the coolant, the temperature ratio of the primary flow to the coolant flow can be increased to 1.5~1.7 (with dry-ice) and 2.1~2.4 (with liquid nitrogen). Fig. 25 shows the temperature ratios (based on average values for each blowing ratio) at different blowing ratios when dry-ice and liquid nitrogen were used, and when neither was used, at $Re \sim 2{,}000{,}000$. It is worth noticing that the temperature ratio κ varies with blowing ratio and Reynolds number when either dry-ice or liquid nitrogen is used. This variation is caused by the change in the performance of the heat exchanger due to the change in the velocity and density of the

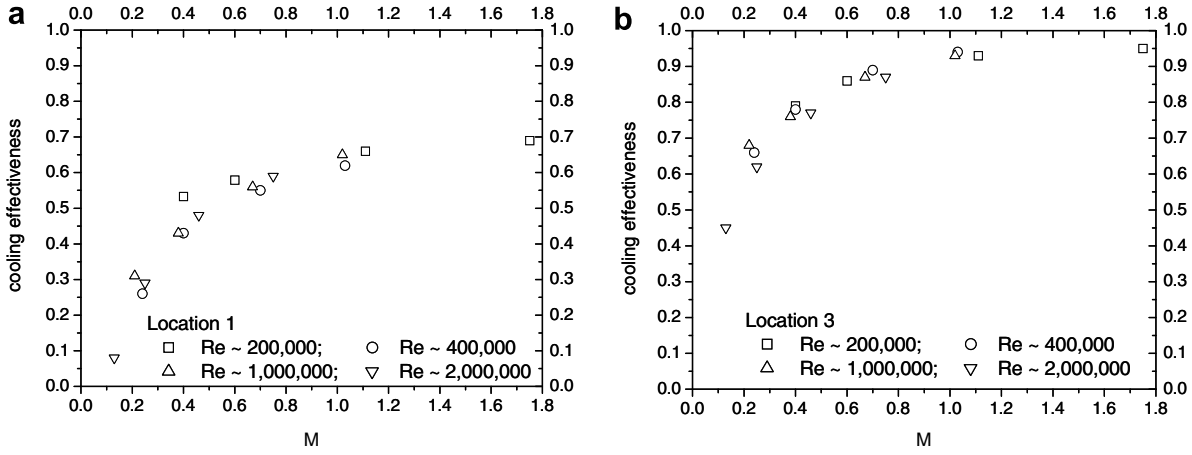

Fig. 22. Cooling effectiveness at different Reynolds numbers (a) location 1; (b) location 3.

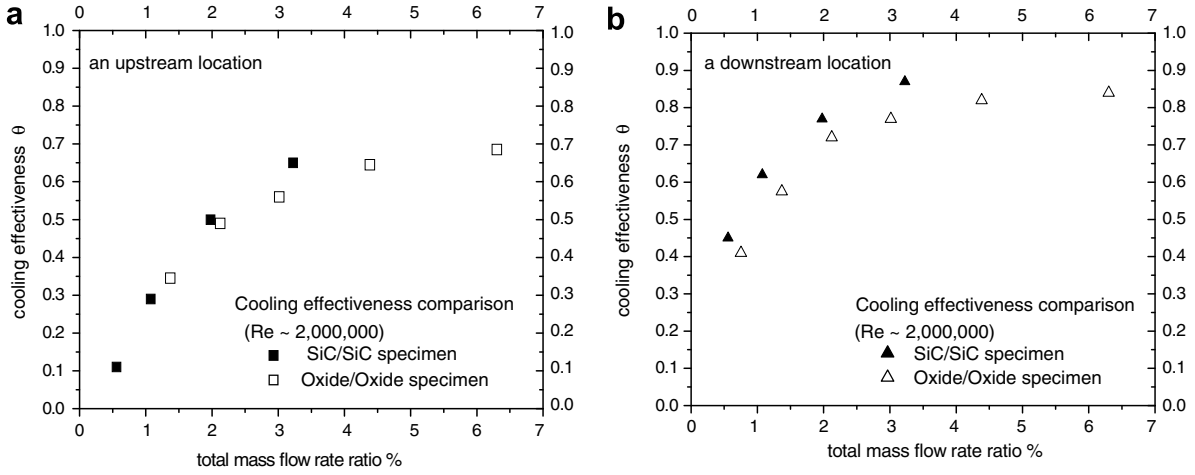

Fig. 23. Comparison of cooling performance between the oxide/oxide specimen and the SiC/SiC specimen (a) at a upstream location; (b) at a downstream location.

coolant flow in the heat exchanger tubing. In Fig. 25, for each case, the temperature ratio varies with blowing ratio and the value increases with blowing ratio except for liquid Nitrogen at a blowing ratio of approximately 0.96. The temperature ratio range for the three cases is $\kappa = 1.1\sim1.2$ (without dry-ice or liquid nitrogen), $\kappa = 1.5\sim1.7$ (with dry-ice) and $\kappa = 2.1\sim2.4$ (with liquid nitrogen), respectively. Although there is a variation with blowing ratio for each case, the difference in κ between the three cases is substantial and the effect of κ on the cooling performance could be studied.

The results for the cooling effectiveness as a function of blowing ratio at $Re \sim 2{,}000{,}000$ and at different temperature ratios are given in Fig. 26. Fig. 26(a) is the cooling effectiveness at location 1 and Fig. 26(b) is for location 3. A decrease in cooling effectiveness with temperature ratio is found for both locations. This effect can be attributed to the decrease in the volume flow rate of the denser coolant at lower temperatures for the same blowing ratio. With less flow volume at the exit of holes, the coolant is qualitatively less effective in covering the downstream surface. The measured temperature profile (shown in a later figure) supports this explanation. If instead the momentum ratio ($I = \frac{(\rho v^2)_c}{(\rho u^2)_\infty}$) is used as the parameter, against which the cooling effectiveness is plotted, the results shown in Fig. 27(a) and (b) are obtained. The comparison between Fig. 26(a) and Fig. 27(a) at location 1 as well as that between Fig. 26(b) and Fig. 27(b) at location 3 show that the collapse of the data using I as the parameter is much better than using M. From the point of view of the entrainment in the far field of a jet, this result is not unexpected. Based on the present cooling cases, the momentum ratio I is a better parameter than the blowing ratio M for the collapse of the effects of temperature ratio.

Fig. 28(a) and (b) gives the normalized temperature profiles η defined by Eq. (3) and the temperature gradient $-\frac{\partial\eta}{\partial y}$ for two temperature ratios ($\kappa \sim 1.2$ and $\kappa \sim 2.3$) and at a large blowing ratio. From the previous discussion, at approximately $M \sim 0.8$, a local coolant film is being established over the surface for the small temperature ratio case, which is confirmed here by the measured temperature profile and its gradient near the wall. By contrast, a similar trend in the temperature profile is not observed for the large temperature ratio case at $M \sim 0.75$. This indicates that a local coolant film has not yet been formed over the surface, at a blowing ratio of 0.75, due to the reduced coolant volume flow rate for the denser coolant at approximately the same blowing ratio (Note: the volume flow rate for the large temperature ratio case is approximately one half of the volume flow rate for the small temperature ratio case).

4.2.4. Duplication of a convective cooling process for real combustor flow conditions

As discussed in the introduction, parameter scaling is used for a duplication of the near-wall cooling process (Reynolds number, density and density ratio) for representative combustor flow conditions. They are obtained by operating the tunnel at a pressure of 10 atm, a free stream temperature of 390 K and at a speed of 18 m/s with coolant injected at a temperature of ~170 K. This leads to a Reynolds number, based on the incoming turbulent boundary layer development length, of approximately 3,600,000 and a temperature ratio of approximately 2.3. The measured temperatures as a function of time at a blowing ratio of 0.4 are shown in Fig. 29 (a) and from the figure, a new thermal equilibrium is reached at approximately $t = 75$ s, which is 30 s after the initiation of injection. This injection of coolant is initiated at $t = 45$ s and stopped at $t = 140$ s and the whole injection process lasts for approximately 100 s. Fig. 29 (b) gives the change of the measured temperature ratio κ with time and a variation of less than 0.1 in κ is found during the injection process from $t = 75$ s to $t = 140$ s. Fig. 29 (c) shows the cooling effectiveness at different locations as functions of time and Fig. 29 (d) is the calculated blowing ratio.

Fig. 30 gives the results for the cooling effectiveness measured at the four streamwise locations (indicated in Fig. 20) for eight blowing ratios. At the highest blowing ratio ($M > 1.0$) in the figure, a cooling effectiveness of ~0.65 can be achieved for the most upstream location (location 1) and ~0.9 for the most downstream location (location 4). It is found in Fig. 30 that the cooling effectiveness continues to increase at $M \geqslant 0.7$, which as discussed in Section 4.2.3, indicates that a local cooling film has not yet been fully established above the surface for the large temperature ratio ($\kappa \sim 2.3$) cases.

Considering that the percentage of hole area on the surface is only 4.5%, the cooling system is found to be relatively efficient since the required coolant mass flow rate per unit surface area is only approximately 5% of the mass flow rate per unit area of the primary flow in order to obtain a cooling effectiveness of 0.65 at the 1st row of holes and 0.93 at the 11th row of holes.

5. Conclusions

In this paper, multi-hole cooling for integrally-woven, ceramic matrix composite walls with different injection holes and ceramic materials has been studied. Based on the experimental results, several conclusions can be drawn:

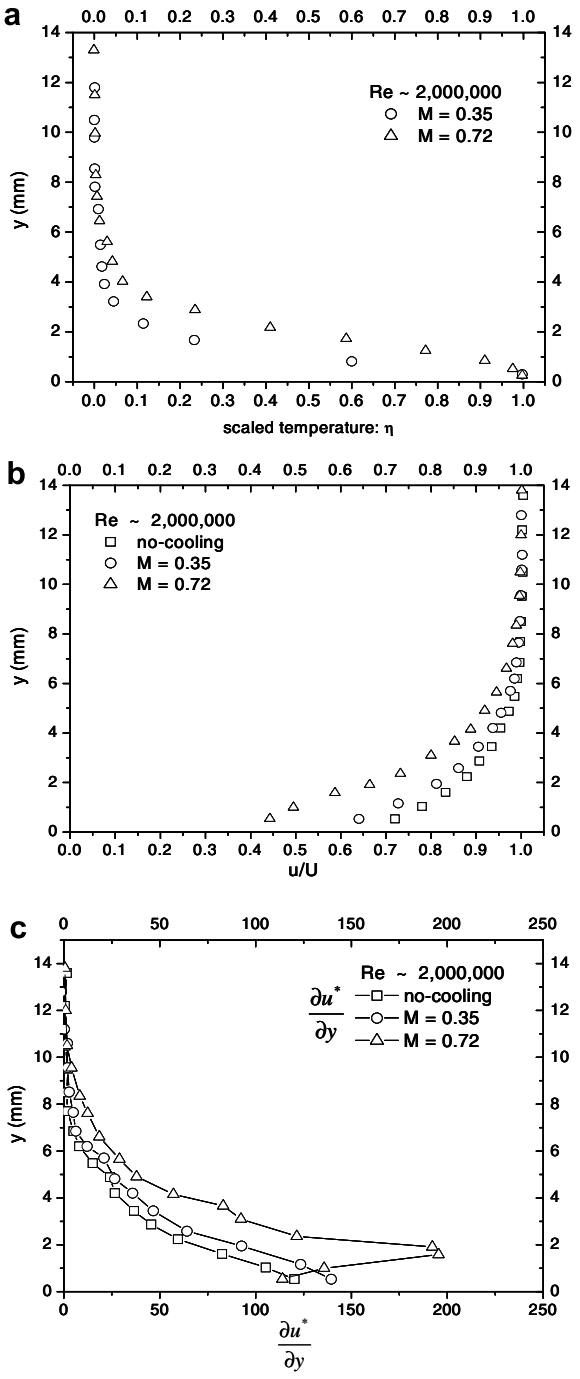

Fig. 24. Normalized temperature & velocity profiles and velocity gradient with and without cooling at $Re \sim 2{,}000{,}000$ (a) temperature; (b) velocity.

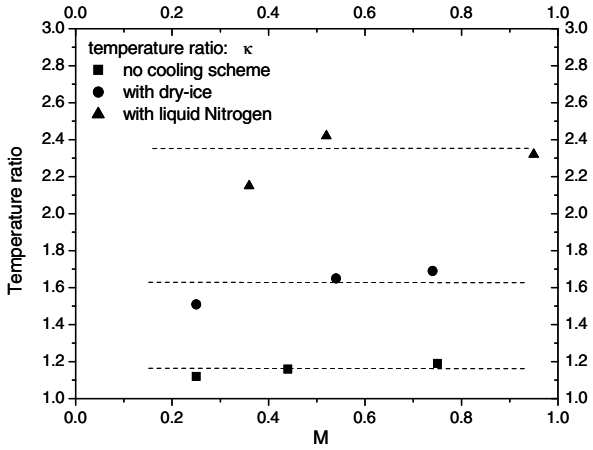

Fig. 25. Temperature ratio of the primary flow to the coolant with different heat exchanger bath temperatures for $Re \sim 2{,}000{,}000$.

(1) The special purpose heat transfer tunnel is an effective facility for a multi-hole cooling study of representative walls. A wide range of Reynolds numbers can be obtained by simply adjusting the tunnel pressure and tunnel speed, and large temperature ratios, representative of gas turbine applications, can be obtained by a coolant flow injection system with a heat exchanger. With parameter scaling, the heat transfer tunnel enables duplication of key parameters of a multi-hole cooling system for real combustor flow conditions (Fig. 29).

(2) Results of the measured surface temperature indicate high cooling efficiency for both specimens (Figs. 12 and 21). The SiC/SiC specimen with pairs of oblique holes and larger thermal conductivity shows a better cooling efficiency than the oxide/oxide specimen with short normal holes (Fig. 23).

(3) At low temperature ratios for both specimens, it is found that for a blowing ratio larger than approximately 0.2, there is no significant increase in the cooling effectiveness in the streamwise direction downstream of approximately the 5th spanwise row of holes, which indicates a relatively uniform temperature distribution on the cooling surfaces (Fig. 12 and 21).

(4) At low temperature ratios for both specimens, the results for the cooling effectiveness as a function of blowing ratio (Figs. 13 and 22) show that there is no significant improvement at blowing ratios larger than 0.7∼0.8, which suggests a local coolant film has been formed above the surface.

(5) The measured temperature profiles at low temperature ratios show a local approach towards zero temperature gradient at the wall for large blowing ratios, which support conclusion 4 (Figs. 14, 15 and 24). However, for large temperature ratio cases, at the same blowing ratio, the temperature gradient in the profile near the wall does not approach zero, because the volume flow rate is less for the denser coolant (Fig. 28).

(6) A Reynolds number dependence is found for the oxide/oxide specimen. The cooling effectiveness decreases as Reynolds number increases. However, this effect is only important for small to moderate blowing ratios ($M < 0.6$); for large blowing ratios, it diminishes (within the measurement error) (Fig. 13). It can be explained by a combined effect of the heat conduction in the wall and the heat convection in the backside coolant flow. For the SiC/SiC specimen, no significant Reynolds number dependence is found, which is the result of a larger thermal conductivity and a thinner wall (i.e. smaller Biot number) (Fig. 22).

(7) From the results for the SiC/SiC specimen, the cooling effectiveness at a given blowing ratio is found to decrease as temperature ratio increases (Fig. 26). It can be explained by the reduced volume flow rate of the denser coolant at the same blowing ratio. If instead the momentum ratio I is used as the parameter, the dependence of the cooling effectiveness on the temperature ratio diminishes significantly (Fig. 27).

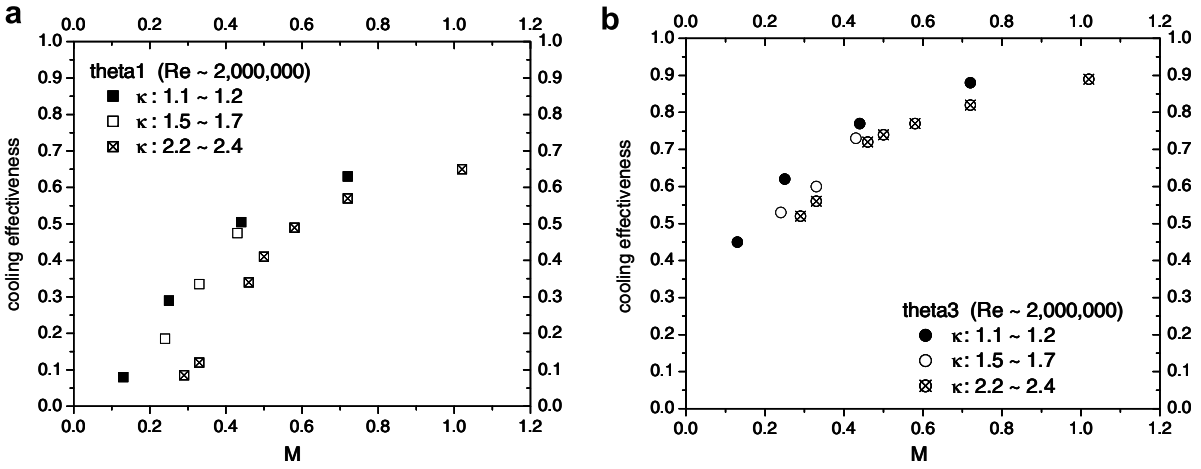

Fig. 26. Cooling effectiveness vs. blowing ratio M at different locations at $Re \sim 2{,}000{,}000$ (a) location1; (b) location 3.

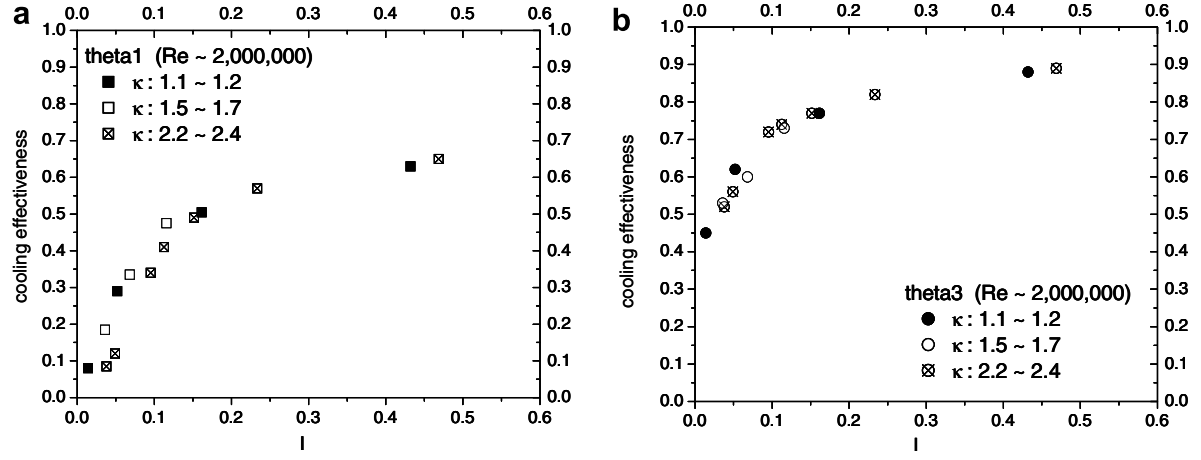

Fig. 27. Cooling effectiveness vs. momentum ratio I at different locations at $Re \sim 2{,}000{,}000$ (a) location1; (b) location 3.

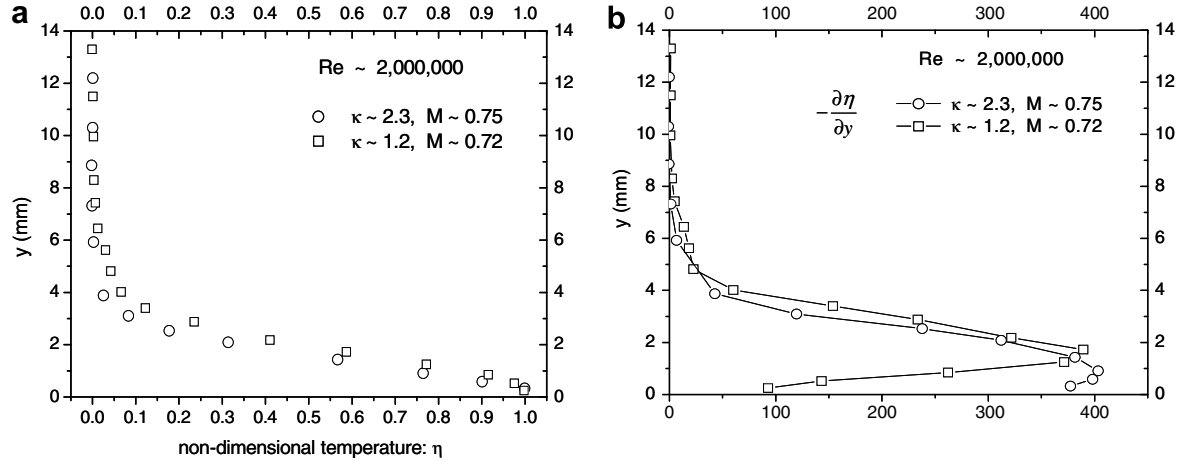

Fig. 28. Comparison of the normalized temperature profile and its gradient at different temperature ratios at $Re \sim 2{,}000{,}000$ (a) temperature; (b) temperature gradient.

(8) The cooling effectiveness for the present multi-hole SiC/SiC specimen obtained from a duplication of multi-hole cooling for representative combustor flow conditions shows high cooling efficiency. A coolant mass flow rate of approximately 5% of the free stream mass flow rate per unit area is required to achieve a cooling effectiveness greater than 0.6 after the first row of holes and greater than 0.9 after the 11th row of holes (Fig. 30).

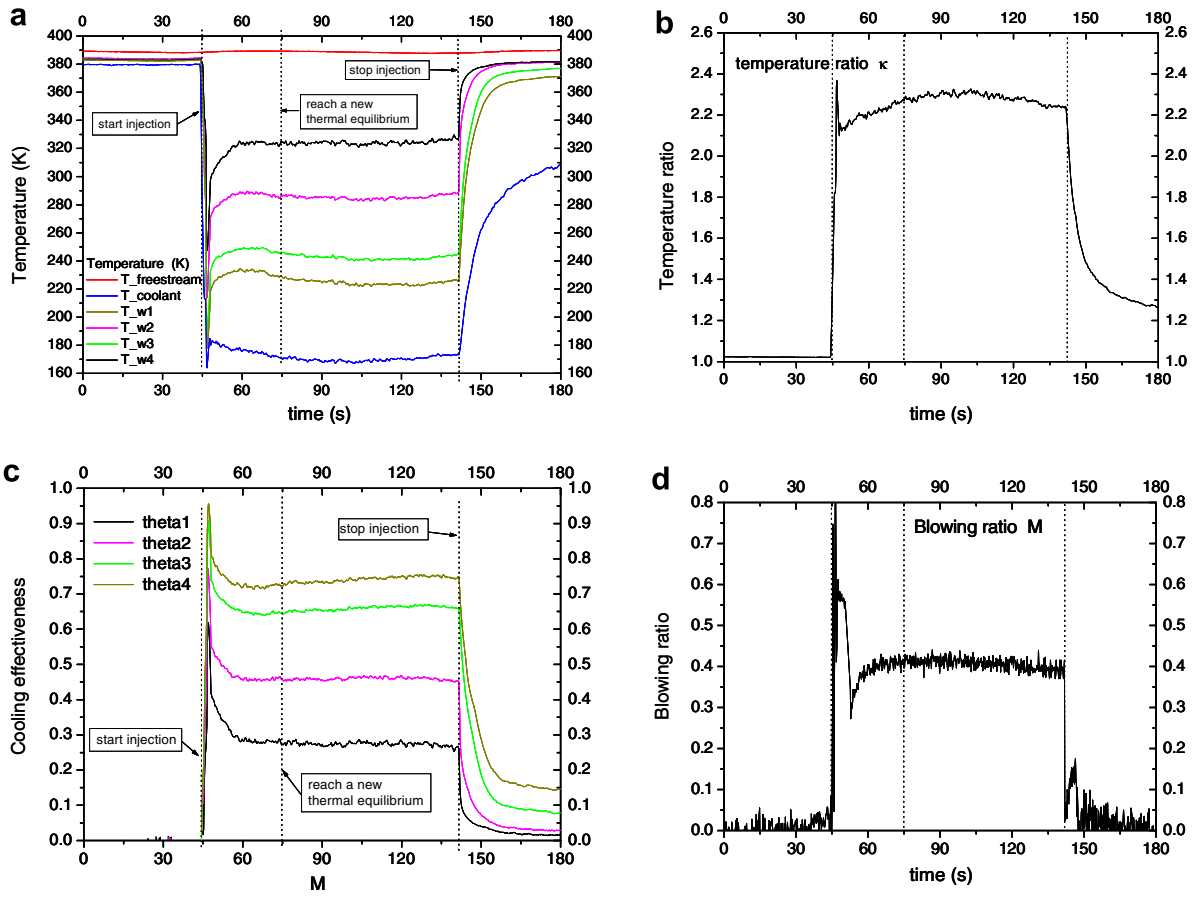

Fig. 29. Measured pressure, temperature etc. for one injection process (a) temperatures; (b) temperature ratio; (c) cooling effectiveness; (d) blowing ratio; ($Re \sim 3{,}600{,}000$, $\kappa \sim 2.3$ and $M \sim 0.4$).

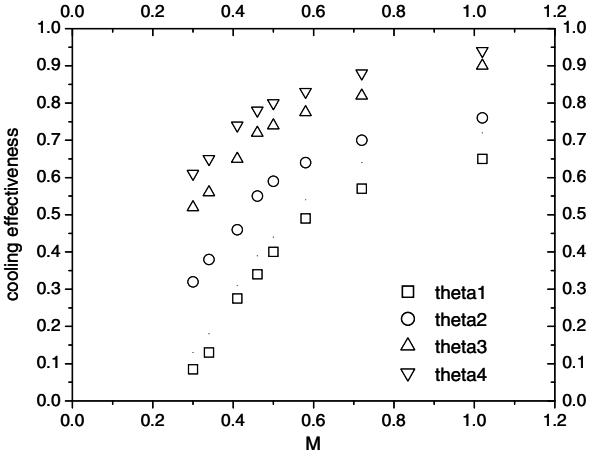

Fig. 30. Cooling effectiveness at different streamwise locations for the duplication of combustor flow conditions (no radiation) ($Re \sim 3{,}600{,}000$, $\kappa \sim 2.3$).

Acknowledgements

The authors thank David Marshall and Brian Cox from the Rockwell Science Center for providing the woven ceramic matrix composite specimens and AFRL, Rockwell Science Center and TK Engineering for their support and interest in this work.

References

[1] B.N. Cox, J.B. Davis, D.B. Marshall, Q.D. Yang, Integral Textile Ceramic Composites for Turbine Engine Combustors, GT-2002-30056, ASME Turbo Expo 2002, Amsterdam, The Netherlands.
[2] J.M. Mehta, D. Shouse, B. Cox, D. Marshall, D. Burrus, B. Duncan, Innovative SiC–SiC Ceramic Liner for The Trapped Vortex Combustor (TVC) Concept, AIAA-2004-689.
[3] F. Zhong, G.L. Brown, Experimental and Numerical studies of multi-hole cooled ceramic matrix composite liners, AIAA-2005-0184.
[4] F. Zhong, G.L. Brown, A 3-dimensional, coupled, DNS, heat transfer model and solution for multi-hole cooling, Int. J. Heat Mass Transfer 50 (2007) 1328–1343.
[5] J. Mehta, D. Shouse, G. Holloway, B. Cox, D. Marshall, Optimization of Integrally Woven SiC–SiC Ceramic Combustor Liner Thermal Parameters, AIAA-2004-4081.
[6] F. Zhong, An Experimental and DNS Numerical Study of Multi-Hole Cooling, Ph.D. Dissertation, Princeton University, 2007.